16th ICAAR LISBOA 2020-2022

16th International Conference on
Alkali-Aggregate Reaction in Concrete
Lisboa | LNEC | Portugal | 31 May - 2 June 2022

http://icaar2020-2022.lnec.pt

Evolution of alkali-silica reaction cracks and products in concrete at the meso-scale studied by X-ray micro-tomography

Mahdieh Shakoorioskooie [1, 2, 3], Michele Griffa [1], Andreas Leemann [1], Robert Zboray [3], Pietro Lura [1, 2]

(1) Concrete and Asphalt Laboratory, Empa, Swiss Federal Laboratories for Materials Science and Technology, CH-8600 Dübendorf, Switzerland

(2) Institute for Building Materials (IfB), ETH Zürich, Stefano-Franscini-Platz 3, CH-8093 Zürich, Switzerland

(3) Center for X-ray Analytics, Empa, Swiss Federal Laboratories for Materials Science and Technology, CH-8600 Dübendorf, Switzerland

Abstract

Significant research efforts have been dedicated to understanding the evolution of damage produced in concrete by the alkali silica reaction (ASR), with the final goal of predicting its development in real-world structures. Nevertheless, the mechanisms for aggregate swelling, followed by its cracking, are still only partially understood. In this study, we present a non-destructive, time-lapse characterization of ASR-caused cracking in concrete at the meso-scale using X-ray micro-tomography (XMT). To accelerate ASR in the laboratory, a specific protocol was executed comprising the immersion of the specimens in an alkaline solution. The tomographic imaging of the ASR-induced cracking was performed at the beginning of the ASR acceleration and continued at specific time points later on (12, 20 and 36 weeks). To make the ASR products visible in the tomograms, caesium was used as a tracer to increase the X-ray contrast. Finally, 3D image analysis workflows were applied to investigate ASR cracking and identify ASR products. Our results confirm the usefulness of caesium for X-ray absorption-based "labelling" of ASR products, without any spurious perturbation of the ASR process. Such labelling allowed observing an extensive and long range filling up of the pore space by the ASR products. Not only cracks but also other types of pores were filled by the products, starting from those at the aggregate-cement paste interfaces. The observed long range transport of products both outside and inside the aggregates suggests the products having significant viscoelasticity, which still requires characterization, if progress in understanding and model ASR damage wants to be achieved.

***Keywords**: Concrete; X-ray tomography; Alkali silica reaction; Time-lapse measurements; image processing*

1. INTRODUCTION

One of the most important durability issues regarding concrete structures is the alkali-silica reaction (ASR). It can lead, to severe damage for critical infrastructure such as dams and bridges. ASR is caused by reaction between metastable silica (which exists in most of the aggregates) and a highly alkaline pore solution [1]. The formation of reaction products gives rise to cracks, first originating within the aggregates, then propagating into the cement paste. The cracking results from dimensional changes of the aggregates. The reaction products typically occupy more space than the unreacted silica. In the long term, ASR cracking usually leads to macroscopic crack patterns observable on the surface of concrete structures usually several years after construction [2–4]. ASR cracking was first identified seven decades ago [2]. Since then, it has been widely investigated from a variety of perspectives and by implementing several characterization tools and methods [1]. However, there are still many unknown aspects. Some details about the chemo-mechanics of ASR product formation and consequent cracking have already been reported. However, the exact mechanisms of the initial product formation, the corresponding, coupled aggregate cracking and the product redistribution are still not fully understood [5, 6]. Electron and optical microscopy have been extensively used to visualize ASR products and cracks [1]. However, as for any other destructive characterization technique, they do not allow tracking damage evolution repeatedly and consistently in the same exact specimens, due to the destructiveness of the respective specimen preparation. Thus, a statistically representative time-lapse characterization of ASR damage is unfeasible using such methods. On the contrary, to achieve a better understanding about

ASR damage, a continuous, non-destructive characterization is extremely important. X-ray micro-tomography (XMT) can perfectly serve this purpose. XMT has already been used to study in time-lapse mode the ASR cracking in laboratory-accelerated specimens [7–11]. Standard XMT easily allows for imaging cracks above the spatial resolution which can be achieved with the used measurement configuration and specimen size. However, it is limited in identifying ASR products, due to the lack of image contrast between them and the other concrete components. A similar issue affects also scanning electron microscopy (SEM). In both standard XTM and SEM, the small differences in mass density and effective atomic number for products and other phases bear little difference in the interaction response (photoelectric absorption and electron back-scattering and/or secondary emission, respectively) of the illuminated specimen with the illuminating radiation beam (X-ray and electron, respectively). This intrinsic limitation in distinguishing the ASR products from other material phases, just based on contrast, is specifically significant at the early ASR times. Initial ASR products do not differ yet even in morphology from the unreactive silica. On the contrary, the secondary ASR products, formed after the initial cracking, have typical morphological features that make them clearly distinguishable in SEM from other phases, once they can be spatially resolved [5]. Nonetheless, that does not apply to X-ray imaging, regardless of the reaction stage. Such non-destructive 3D imaging technique typically cannot achieve enough spatial resolution to allow distinguishing morphological features of ASR products.

One of the well-established approaches to identify, with conventional, laboratory-based XMT, a phase which does not have different enough X-ray photoelectric absorption, compared with its surroundings, is to add a so called "contrast agent". The chosen agent is typically capable of selectively "binding" (chemically or in other ways) to the target phase and has high atomic number or mass density [12, 13]. This increases the effective photoelectric absorption of the target. For ASR products, one way of achieving that is to have a pore solution where part of the alkali ions are of atomic species with high atomic number. Alkali ions become naturally incorporated in the ASR products but less so in the cement hydrates [14]. The pore solution of concrete contains sodium and potassium. By adding an alkali with higher atomic number to the mixing water, it is possible to selectively increase the photoelectric absorption of the ASR products due to their alkali uptake. Caesium (Cs) is a suitable candidate for this purpose, due to its higher atomic number compared to sodium and potassium. Furthermore, the hydrated radius of Cs ions is in the same range as the one of potassium. Potassium is another alkali metal typically participating in ASR [15]. Recently, Leemann *et al.* [14] showed, for the first time by SEM, that Cs ions are actually bound to ASR products and that they significantly increase the electron back-scatter contrast of the ASR products. Here, we show, for the first time, similar results for 3D images obtained by XTM. The enhanced contrast of the Cs-containing ASR products allows characterizing the ASR damage evolution, both in terms of crack network evolution and coupled mass transport of the products.

2. EXPERIMENTAL METHODOLOGY

2.1 Specimen preparation, ASR acceleration and chemo-mechanical characterization of ASR products

Two types of concrete specimens were produced, the reference ones (C-Ref), without caesium addition, and the ones with caesium addition (C-Cs). All specimens were cast using 440 kg/m^3 of Portland cement (CEM I 42.5 N) and a water-to-cement (mass-)ratio (w/c) of 0.50. The aggregates used came from Praz (southwest of Switzerland). They are of alluvial origin. They mainly consist of gneiss and quartzite. An aggregate mass of 1790 kg/m^3 was used in the mix, with the following grain size distribution: 0-4 mm, 40 mass-%; 4-8 mm, 25 mass-%, 8-11.25 mm, 35 mass-%. For the C-Cs specimens, 1.91 kg of $CsNO_3$ *per* 100 kg cement was added in the mixing water. Six prisms with size of 40×40×160 mm^3 were cast from both mixtures. The specimens were kept at 100% relative humidity (RH) for 24 h. They were then unmoulded and immersed in an alkaline solution (0.3 M KOH, 0.1 M NaOH) at a temperature of 40 °C.

Mass and length changes were regularly measured at specific time points. A FEI Quanta 650 scanning electron microscope, equipped with an energy dispersive X-ray spectroscopy (EDS) detector (Thermo Noran Ultra Dry 60 mm^2) and with the Pathfinder X-Ray Microanalysis software, was used to study the microstructure of the ASR-damaged specimens and the chemical composition of the ASR products. An acceleration voltage of 12 kV for the electron beam was selected for both back-scatter-electron images and EDS point analysis.

2.2 Temporal monitoring of ASR damage by X-ray micro-tomography

Time-lapse XMT was performed at specific time points on specimens of both types. 3 specimens from each type were used to evaluate the consistency of the results. XMT was carried out using an EasyTomo XL- Ultra tomograph (RX Solutions, Chavanod, France). Such instrument is based upon a micro-focus, direct transmission X-ray source and a flat panel X-ray detector. The X-ray source (Hamamatsu L10711-02) is equipped with a LaB_6 filament and a 1 µm-thick W target deposited on a 500 nm-thick diamond support, which allows achieving sub-micron X-ray source focal spot size. The X-ray detector (by Varian) consists of a 2D array of amorphous Si pixels (1920 × 1536), each with physical size of p = 127 µm, covered with a thin layer of CsI. The latter, as a scintillator for the X-ray photons, converts them into visible light photons, which are then detected by the amorphous Si pixels. XMT was performed with 90 kV and 150 µA X-ray source settings (using a 230 kV X-ray source). The specimen-to-source distance (d_{sS}) was set to 113.63 mm and the source-to-detector distance (d_{Sd}) was 410.16 mm. A region of interest (ROI) with size 40×40×50 mm^3 was scanned by XMT. The geometrical magnification, $M = {d_{Sd}}/{d_{sS}}$, attained in the raw 2D projection images (called “radiographs”) of the specimen on the detector and due to the X-ray cone beam geometry, was thus approximately 3.6, leading to an effective voxel size of $\tilde{p} = {p}/{M} \cong 35$ µm for the final tomograms. The number of radiographs acquired during each tomography measurement was 3600 over 360° of specimen rotation. Each tomogram was reconstructed from such set of corresponding radiographs with a GPU-optimized cone beam filtered back-projection algorithm [16] available in RX Solutions’ software (XACT Ver. 1.1). The effective spatial resolution of the tomograms (defined as approximately twice the effective voxel size) was estimated to be about 70 µm. To enhance the signal-to-noise ratio of the tomograms and enabling a better feature detection in the concrete structure, a 3D anisotropic diffusion filter was applied to the raw tomograms. This filter is based on an edge-preserving denoising algorithm [17, 18] which was implemented as an ImageJ plugin in the Xlib library [19].

A 3D image analysis protocol was developed and implemented in the Avizo software by ThermoFisher for identifying ("segmenting") the voxels where cracks and the ASR products were located, respectively.

First of all, the air-filled voxels surrounding the specimens (empty region around the specimen in the tomograms) were excluded from the analysis. Secondly, all the tomograms obtained, for each given specimen, at distinct time points were rigidly aligned (rigidly "registered") with respect to the tomogram at the first point in the time series. The rigid body registration was performed using the Python interface of the SimpleElastix image registration library [20], which is an extension of SimpleITK (a simplified, open-source interface to the Insight Segmentation and Registration Toolkit) [21]. A multi-resolution rigid body registration based on a mutual information image similarity metric was implemented. Such registration was performed to correct for any human errors in repositioning each specimen on the tomograph's specimen holder at each successive time point.

The crack segmentation started with applying the Black Top Hat (BTH) morphological transform to each filtered and registered tomogram, followed by a further segmentation of the BTH transform's output and by a final "image cleaning" post-processing (CPP) step. The BTH transform has been already used for segmenting crack-like features [22]. It allows for finding local voxel value minima in the tomograms, corresponding with the centre regions of the pore space, typically characterized by very small voxel values compared with the surrounding material phases. We used Avizo's implementation of the BTH transform. Since the output of the BTH transform is a 3D image with a continuous range of voxel values, indicating a sort of likelihood degree of having a local minimum at the voxel position, only voxels with value within a certain range (or thresholds) were selected. This resulted in a so called "binary tomogram", i.e., a tomogram whose voxels have only two possible values: either 255, if the voxel was classified as belonging to the pore space, or 0, if not. Such a binary tomogram is a 3D spatial map of segmented pore space (including cracks). A following CPP step was implemented to distinguish between actual cracks and other pore space regions, e.g., air voids, irregular pore patches, aggregate dissolution-created small pores. Such pore space regions are typically rather isotropic in shape, compared with cracks. To exclude them from the binary tomogram, a feature-based operation was implemented. It consisted in computing the degree of sphericity of each separated pore region and in excluding those with values larger than a chosen threshold. The degree of sphericity was defined as the ratio of the surface area of a perfect sphere, with volume equal to the one of the region, to the surface area of the region itself. Degree of sphericity values close or equal to 1 are associated to very spherical regions, while crack-like regions are characterized by a sphericity value much less than one [23]. The resulting binary tomograms thus contained only pore space regions considered as "cracks".

Similar to the pore space segmentation by the BTH transform, it is possible to segment the voxels associated with the Cs-doped ASR products by looking for spatial regions in the tomograms where local maxima are located. Such local maxima search can be performed with a white top hat (WTH) transform. However, other natural regions with similarly high voxel values coexist within the aggregates. An example are regions containing minerals with X-ray photoelectric absorption as large as that of Cs-doped compounds. Due to this coexistence, the sole implementation of a segmentation workflow, similar to what described before and used for the crack segmentation but starting with a WTH transform, does not allow to segment only ASR products. Therefore, a more sophisticated procedure was used to distinguish the ASR products from other features with high X-ray attenuation. This consisted of performing affine registration of each tomogram to its corresponding time-reference one. Then, the affine registered tomogram was subtracted from the reference one to obtain a new tomogram in which only the new features, created at successive time points and by the ASR damage, are visible. Among such new features there are the ASR products, which could then be segmented by a workflow similar to the crack segmentation workflow but based upon the WTH transform. The affine registration was carried out also by using the Python interface of SimpleElastix, still through a multi-resolution scheme and by using mutual information as image similarity metric.

3. RESULTS

We investigated both types of concrete specimens (C-Ref and C-Cs) from various points of view, to assess the differences and/or similarities in the ASR evolution mechanisms. One of the most important aspects was any difference in the mass and length changes, in the absence and in the presence of the added $CsNO_3$. The ASR products were observed at a length scale of hundreds of nm, by SEM, and their chemical compositions were compared by EDS analysis. Finally, the ASR crack patterns and ASR products' spatial-temporal distribution were analysed qualitatively using XMT. After confirming the existence of similarities between the normal and the Cs-doped ASR products, we exploited their traceability for improving the understanding of and explaining the ASR (damage) evolution over time. In the following sections, each of these aspects are discussed.

3.1 Mass and length change

The relative mass and length changes of C-Ref and C-Cs specimens are shown in Figure 3.1. The relative mass change, Figure 3.1(a), increased continuously with similar trends at early ages of cement hydration. However, after about 8 weeks, the C-Cs specimens showed a higher mass increase than the C-Ref ones, reaching a ≈33% larger value at 36 weeks. The relative length change (Figure 3.1(b)) shows an analogous development as the mass change. However, the length change of concrete C-Cs started to show higher values than those of concrete C-Ref already at 4 weeks, leading, at 36 weeks, to values nearly twice as high compared to those of concrete C-Ref.

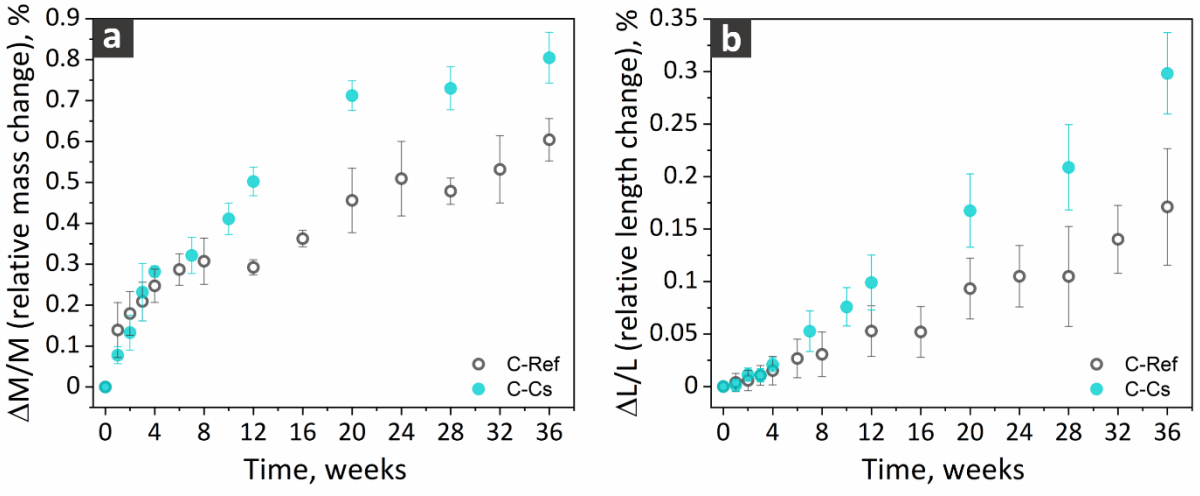

Figure 3.1: Time series of relative (a) mass change and (b) length change of concrete C-Cs and C-Ref specimens. Each marker refers to the sample average value and each error bar refers to the sample standard deviation, the statistical sample consisting of 10 values from 10 distinct specimens.

3.2 Morphology and chemical composition of ASR products

In both concrete mixtures, back-scatter electron (BSE) images were acquired after 20 weeks at locations containing cracks in the interior of aggregates (Figure 3.2). For both types of specimens, it can be observed in Fig. 3.2 that ASR products with analogous plate-like morphology formed. Additionally, plenty of amorphous ASR products were also observed, especially in the cement paste of the C-Cs specimens. The plate-like morphology was recognized only inside aggregates, while the amorphous products occurred both in aggregates and in cement paste.

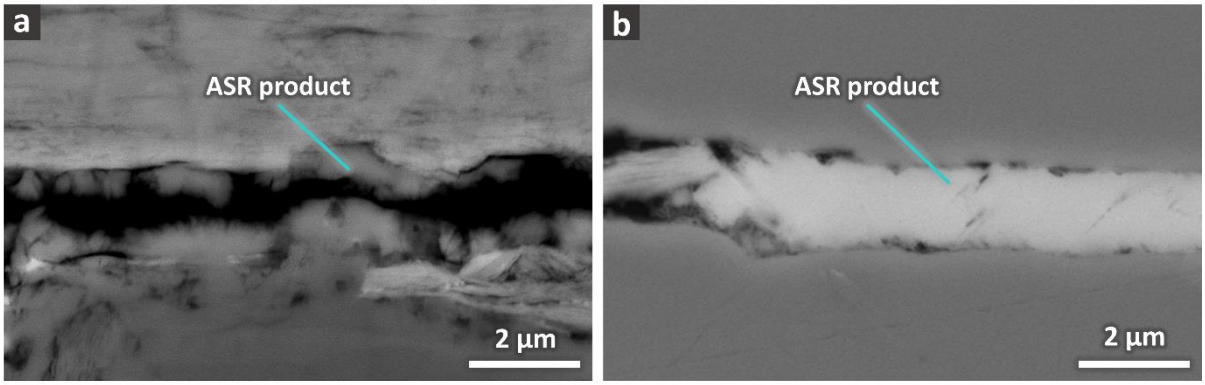

Figure 3.2: Back-scatter electron (BSE) images of cracks filled with ASR products and located inside aggregates of a concrete C-Ref specimen (a) and of a concrete C-Cs one (b), respectively. ASR products in the concrete C-Cs specimen appear clearly brighter due to the increased BSE-contrast.

The ASR products in the C-Ref specimens, Figure 3.2(a), have almost the same pixel, i.e., BSE coefficient, value as the surrounding minerals. Thus, they can be recognized mainly due to the typical plate-like morphology mentioned above. The observed, significant BSE contrast enhancement between the ASR products and the aggregate in the C-Cs specimen, Figure 3.2(b), indicates that Cs was indeed incorporated in the ASR products. This is confirmed by EDS analysis. Assessed qualitatively, a larger relative amount of ASR products seems to be present in the C-Cs specimens compared to their reference counterparts. The average molar ratio of Ca/Si in the ASR products in concrete C-Cs was lower (0.21) than the one of the products in concrete C-Ref (0.28), in agreement with what already observed by Leemann and Münch [14].

3.3 X-ray micro-tomography results

In order to assess qualitatively the extent of ASR damage and its evolution in time, XMT was performed at different time points, until a total time of 36 weeks. At each time point, approximately the same region was imaged for each specimen.

Figure 3.3 shows a small region of interest (ROI) from a single, selected planar cross-section (also called tomographic "slice") from the tomograms of a C-Ref specimen, acquired at distinct time points. The location of the slice in each tomogram is exactly the same. Since the tomograms were rigidly registered, such slice shows approximately the same 2D plane of that specimen. In addition, the ROI from the larger whole slice was chosen as such to better illustrate the evolution of a few specific cracks. The blue arrows superimposed on the slices point to the regions with cracks. The slices from Figure 3.3(a) to Figure 3.3(d) showcase the level of cracking, starting from 4 weeks until 36 weeks, respectively. The reason for starting XMT for the C-Ref specimens after 4 weeks of ASR acceleration was that, based on previous experience, cracks with size above the spatial resolution of the performed tomography (approximately 70 µm) usually appeared after 5 or 6 weeks of ASR acceleration. For the C-Cs specimens, XMT was started exactly from the first day of ASR acceleration, to ensure capturing any possible early age crack nucleation, since the addition of Cs increases the ASR kinetics. Thus, we expected to be able to resolve ASR cracks well before the mentioned 4 weeks.

Crack-like pores observed at 4 weeks (Figure 3.3a) in one C-Ref specimen were mainly located within the aggregates. These pores could be considered either as natural pores, e.g., grain boundaries, or formed during the aggregate production, e.g., actual cracks. They could indeed be observed as well in the tomograms of the C-Cs specimens at the first day of ASR acceleration. Thus, their existence independently of the ASR could be confirmed. After 12 weeks, 20 weeks and 36 weeks (Figures 3.3(b)

to Figure 3.3(d)) some new pores with crack-like features became visible in the considered C-Ref specimens as well as in other ones. It is evident in Fig. 3.3 that such cracks gradually increased in length and/or width. The corresponding expansion values at each of these time points are marked with green stars on the expansion curves in Figure 3.1(b). The increased expansion positively correlated with the appearance of such cracks. Due to similar X-ray photoelectric absorption cross-section values, ASR products, aggregate and hydrated cement phases have similar voxel values in the tomograms. Thus, the only change due to ASR and observable in the tomograms is the appearance of cracks as features with much lower voxel values than the solid material phases. No ASR products inside the cracks can be resolved in the C-Ref tomograms, because of a combination of too low spatial resolution (the crack width was typically close to the spatial resolution of the tomograms) and the rather small X-ray photoelectric absorption of the ASR products, compared with that of the aggregates.

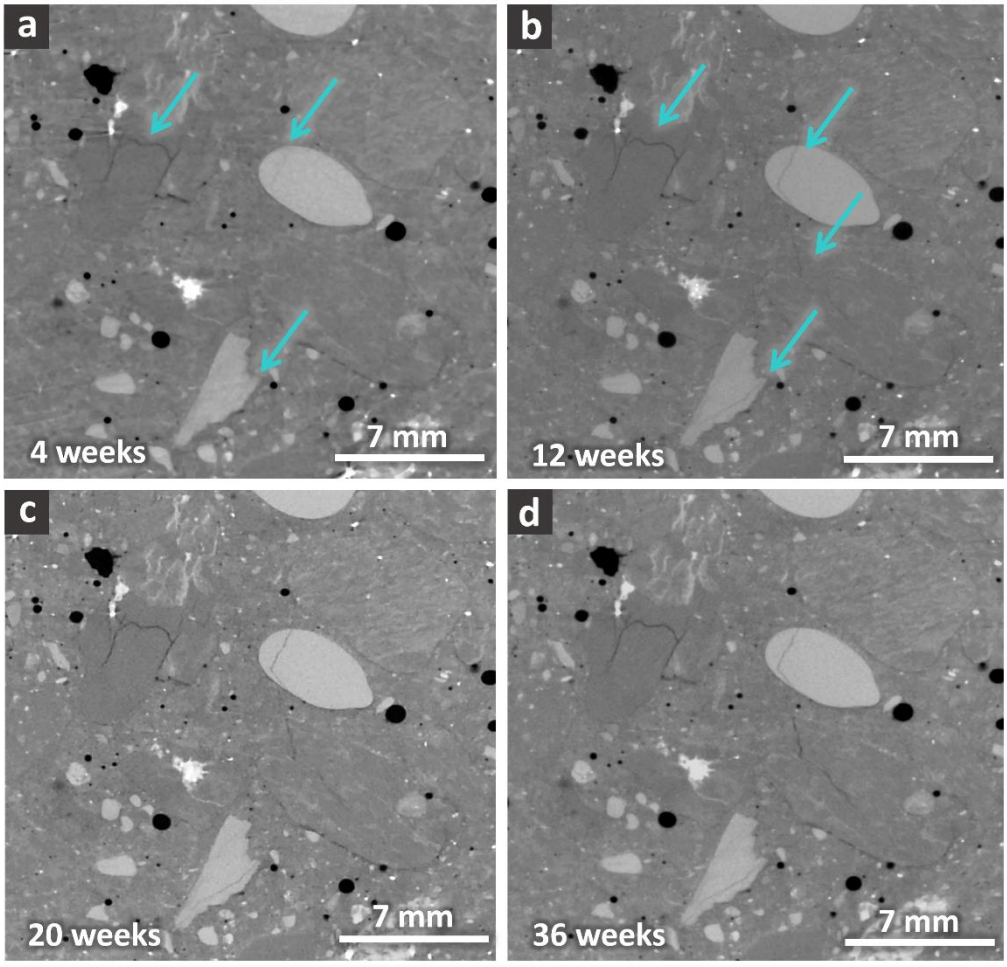

Figure 3.3: Region of interest (ROI) on a selected planar cross-section ("slice") from the X-ray tomograms of one C-Ref specimen, acquired at different time points ((a), 4 weeks, (b), 12 weeks, (c), 20 weeks, (d), 36 weeks). Darker voxels correspond to smaller local electron density, brighter voxels to larger electron density. The arrows highlight pre-existing, crack-like pores inside the aggregates, progressively increasing in length and width during the ASR acceleration, as well as crack-like features newly appearing in the tomograms at a certain time, either completely newly formed or not resolved at previous times.

The visual inspection of the time series of C-Ref tomograms showed that such cracks originated first inside the aggregates, then they propagated into the cement paste, ending up being distributed rather homogenously inside the inspected volume. In order to support the latter conclusion, the cracks in the full tomogram at 36 weeks of one C-Ref specimen were segmented. Their 3D rendering, shown from different points of view, is presented in blue in Figure 3.4. The 3D crack network for the chosen C-Ref specimen and at that time point is shown there as an example of a typical crack network in a quite

heavily ASR-damaged concrete specimen. The crack network consisted of a rather dense combination of long and short cracks. Based on visual observation only, it seems that the crack distribution did not follow a preferred orientation and was homogeneously distributed all over the inspected concrete volume. The presence of such large cracks in the tomograms correlates very well with the considerable overall large expansion levels achieved by the specimens up to 36 weeks.

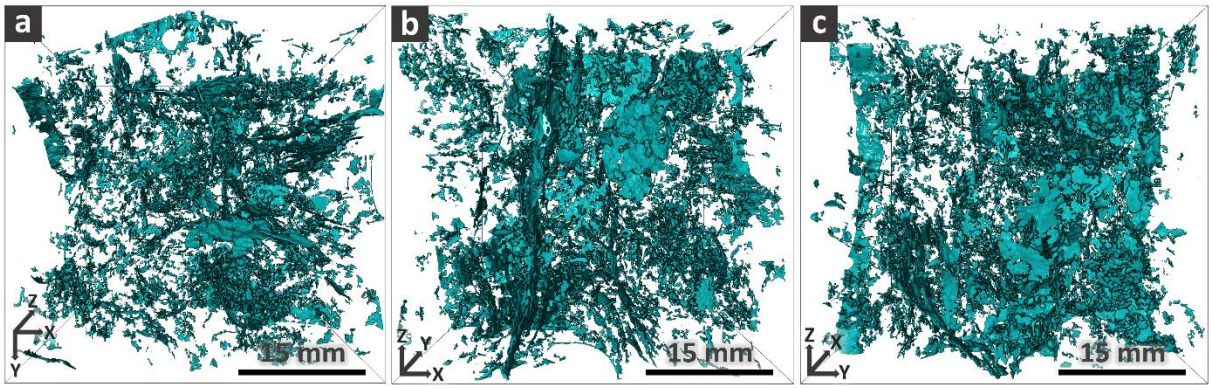

Figure 3.4: 3D rendering of segmented cracks at 36 weeks of ASR acceleration in a C-Ref specimen, shown from three different points of view (see the orientation of the axes of the frame of reference in each image).

The information attainable from the tomograms and from the segmented 3D crack networks provides already some useful understanding about the damage state. However, the actual damage cause, the ASR products, cannot be located, especially at early ASR stages. Cs-doping permits to follow the formation of larger volumes of ASR products, adding important information about the spatio-temporal ASR evolution. Figure 3.5 shows a ROI of a C-Cs specimen's tomographic slice, containing a few aggregates.

The presence of ASR products within the cracks and near the aggregates' boundaries, especially after 20 weeks, is clearly recognizable. The aggregate highlighted in Figure 3.5(a) seems to have contained since the beginning very fine crack-like pores, possibly grain boundaries. After 12 weeks (Figure 3.5(b)) the dominant effect of ASR was mainly filling of the pores close to the aggregate boundaries, particularly the pore space in the Interfacial Transition Zone (ITZ). Subsequently, at 20 weeks, the ASR products got extruded towards the cement paste via the newly created cracks or expanded grain boundaries, Figure 3.5(c). In addition to filling in the cracks in the cement paste on the left-hand side of the centre aggregate, the ASR products also filled the more delaminated ITZ of another adjacent aggregate in its right-hand/bottom side, Figure 3.5(d). At age of 36 weeks, it can be observed that cracks propagated even further, widened up and formed a continuous crack path by interconnection with the other cracks in the cement paste, Figure 3.5(d). The pore space, including the newly created cracks, was filled with further products. Most of the cracks within the aggregates was emptied of any products. At that time, there is almost no sign of larger volumes of ASR products inside aggregates.

In order to achieve better insight into the 3D distribution of ASR products along with the cracks, we performed their 3D segmentation according to what described in Section 2.2. In Figure 3.6, voxels belonging to the cracks are visualized in blue while the ASR product ones are shown in pink. Figures 3.6(a) to 3.6(c) show the 3D renderings of cracks and of products in a ROI of the tomogram of one single C-Cs specimen, viewed from different sides. The frame of reference in each inset specifies the orientation of the volume. By qualitative comparison, the damage density in this C-Cs specimen seems higher than that of the C-Ref specimen shown in Figure 3.4, considering that both datasets where acquired at the same ASR acceleration time. This result agrees with a higher mass gain and length change for the C-Cs specimens. The ASR products tended to fill a large number of pores available next to the aggregates where they were formed. A considerable amount of small aggregates (sand particles) or, at least, their cracks were below the resolution limit. Therefore, the ASR products originated from several of such small particles are visible only when accumulated in pores. The abundance of pores filled with ASR products led to a relatively crowded ensemble of rendered ASR products. Therefore, for clearer illustration, the voxel clusters classified as ASR products were not rendered when having volume below a certain threshold value (0.001 mm^3, which corresponds to very small clusters).

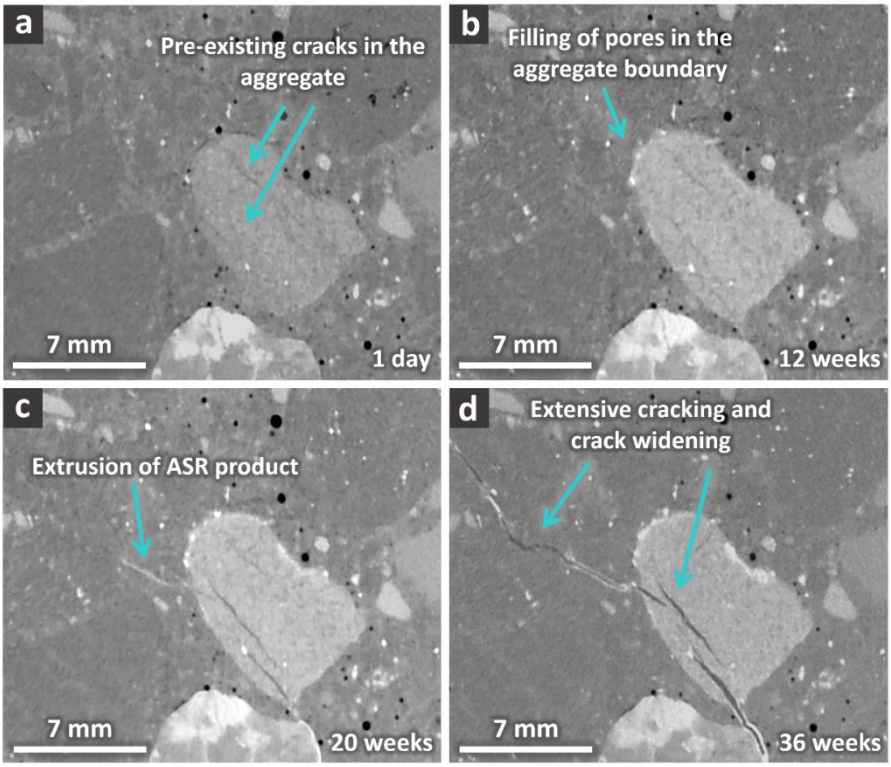

Figure 3.5: Region of interest (ROI) on a selected planar cross-section ("slice") from the X-ray tomograms of one C-Cs specimen acquired at different time points (noted in each inset). Darker voxels correspond to smaller local electron density, brighter voxels to larger electron density values. Some regions containing ASR products appear as very bright, inside or nearby cracks, due to the incorporation of Cs ions that increased significantly the local electron density.

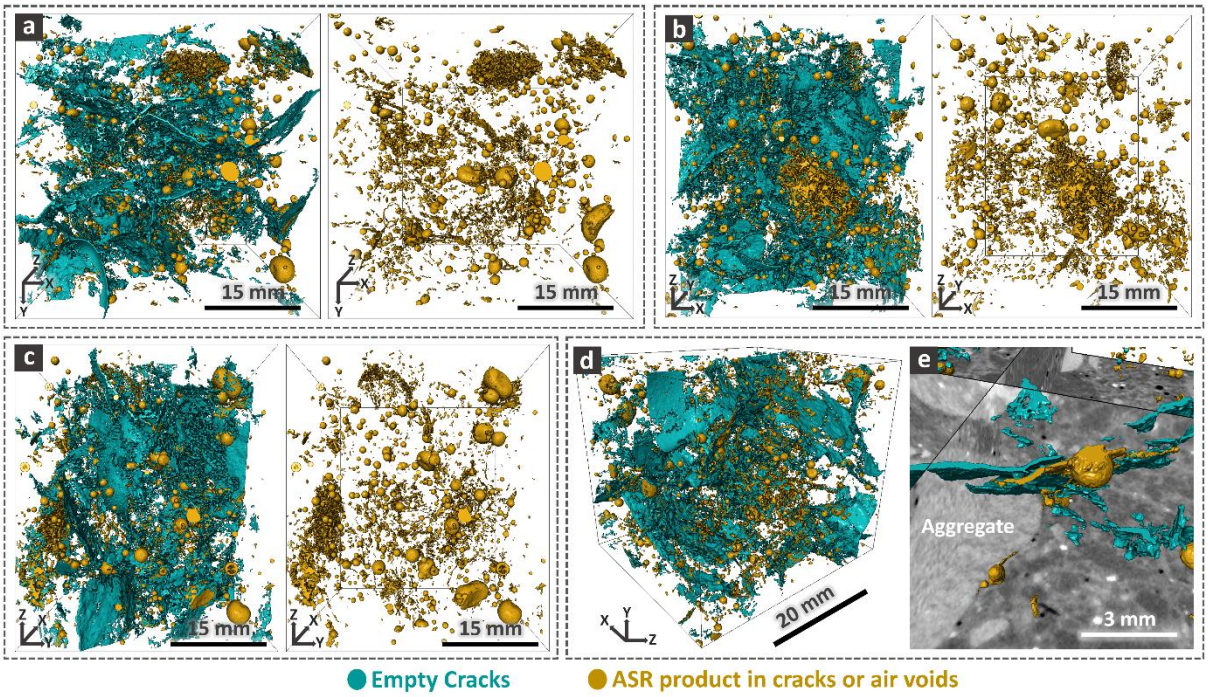

Figure 3.6: (a-d) 3D rendering of segmented empty cracks (in cyan) along with the ASR products (in orange), at 36 weeks and from the tomogram of one C-Cs specimen, shown from four different points of view, denoted in the insets. (e) Zooming in one of the 3D renderings, focusing on a continuous, crack passing through several aggregates and the cement paste.

As a result, a pattern in the spatial distribution of ASR products could be inferred. Indeed, such products were usually located either within or in the nearby of the cracks or filling spherical pores (small and large air voids). They were overall very uniformly distributed all over the inspected volumes (Figure 3.6). Figure 3.6(e) focuses exclusively on one of the continuous cracks, which passed through two large aggregates and ran into the cement paste. Three slices from the actual tomogram, mutually orthogonal to each other, are also shown. They are meant to serve as guidelines to distinguish the locations of aggregates and cement paste. It can be observed that cracks inside the aggregates were mainly empty, while those in the cement matrix were partially filled. In this specific example, it is also observed that most of the ASR products settled inside a large air void located along the large and continuous crack.

4. DISCUSSION

X-ray micro-tomography (XMT) and respective 3D image analysis provided a unique possibility to non-destructively monitor the evolution of the microstructure in ASR-affected concrete. It did not allow resolving features/processes existing/occurring below tens of μm (which could be resolved, on the contrary, by electron microscopy), e.g., primary crack initiation. However, it enables actual time-lapse tracking of ASR cracks larger than a certain size (70 μm, in this work) and their development inside the exact same region of the same specimens. In the C-Ref concrete specimens, with no ASR product "labeling" by Cs ions, only cracks were observed. At the early ASR acceleration times, some inherent (pre-existing) pores with crack-like features could be resolved in the tomograms. They were mainly located in the aggregates. From the electron microscopy investigation of Leemann and Münch [14], inherent pores have been identified as being mainly grain boundaries. These pores of the C-Ref specimens evolved into larger cracks. Furthermore, some of them propagated into the cement paste and, in some cases, contributed to the nucleation of new cracks in other encountering aggregates. Although the observations from the C-Ref specimens provided valuable information about the cracks' spatial and temporal evolution, it is not possible to clearly understand the ASR mechanisms, having only those data. On the contrary, the time series of tomograms of the C-Cs specimens provided an exclusive insight about ASR. At the beginning of the acceleration (1 day-old specimens), similar pre-existing pores as in the C-Ref specimens were also observed in the aggregates. At the early acceleration times, the ASR products accumulated mainly at the ITZ and inside other adjacent pores in the cement paste, next to the aggregates. The observed precipitation of ASR products in such pores suggests that ASR started in some aggregates, including small sand particles. The ASR products were also observed to fill some of the pre-existing crack-like pores at the aggregate boundaries ("delaminated* ITZ). Regardless of the presence or absence of ASR products, the emergence of any new cracks in fine or coarse aggregates was not observed at the early times. This can be due to the spatial resolution limits of the performed XMT. The study by Leemann and Münch [14], where Cs-doping was used for visualize ASR products by SEM, provided valuable hints about the sequence of the processes. In that study, it was observed, at the initial ASR stages, that ASR products started to fill pre-existing pores in the aggregates, advancing as a front from the surface of the aggregates towards their interior. When, at the point of cracking, aggregates formed multiple small cracks, ASR products extruded into the ITZ porosity in the cement paste. Only when one major crack formed instead of multiple small ones, it continued into the cement paste and filled with extruded ASR products. Our time-lapse tomography results cannot confirm the formation of the multiple small cracks observed by Leemann and Münch [14]. However, it clearly shows the formation of major cracks extending into the cement paste at the later stages of ASR. Still, by our data, it was possible to directly observe, at such stages, that the accumulation of products inside cracks proceeded together with further propagation. This kind of extrusion suggests two important features of ASR damage in concrete. Firstly, the long-range extrusion calls for the existence of large stresses inside the aggregates. Secondly, the ASR products seem to possess a viscoelastic behavior leading to their squeezing into the pore space of the cement matrix (cracks included). At later stages, the cracks broadened and propagated even more inside the aggregates, from one side, and into the paste, in the other. Part of the ASR products covered the crack walls inside the aggregates, in addition to those present in the cement matrix. This spatio-temporal pattern was already observed at smaller length scales by Leemann and Münch [14]. Our results not only confirm their results based upon actual time-lapse and fully non-destructive measurements. They also confirm its existence also at larger length scales.

The qualitative comparison of 3D crack networks of C-Ref and C-Cs shows a similar spatial distribution of the cracks. This observation suggests the representativeness and the reliability of using Cs-doped concrete for ASR investigations. Furthermore, the expansion curves of the C-Cs specimens exhibit a

similar trend to the one observed for the C-Ref ones. However, the ASR kinetics is higher for the C-Cs specimens. The resolved cracks exhibit an isotropic orientation all over the specimens, in agreement with the free expansion boundary conditions of the used specimens [24]. Another important characteristic of the resolved ASR cracks in both types of specimens is their homogeneous spatial distribution. Under such free expansion boundary conditions, ASR cracking seems to take place across the full cross-section of a specimen. At very late ASR acceleration times, e.g., 36 weeks, we observed fully inter-connected networks of cracks. Such high level of interconnectedness, when achieved also by ASR-affected concrete in a real-world structure, may lead to very large increases in permeability, thus further reducing the material's durability.

5. CONCLUSIONS

We performed time-lapse X-ray micro-tomography (XMT) on two sets of concrete specimens cast with highly ASR-reactive aggregates. In one set, $CsNO_3$ was added to the mix design in order to increase the image contrast of ASR products to the other material phases, as compared to standard XMT 3D images (tomograms), thus to enhance their identification. In contrast to SEM, XMT is fully non-destructive. As such, it can complement SEM investigations by providing 3D information on the spatial-temporal evolution of both ASR cracks and ASR products. Our results provide for the first time a unique insight not only into the evolution of ASR cracks in concrete but also into the transport of the ASR products.

The most important highlights of this study are:

a) Cs, which gets incorporated into ASR products [14], increases their X-ray attenuation above the values of the aggregates and of the cement paste;

b) due to this increase in X-ray attenuation, ASR products can be identified and segmented in X-ray tomograms;

c) concrete specimens cast with Cs show very similar macroscopic and microscopic ASR damage patterns, except for faster kinetics; thus, specimens cast with Cs addition can be used in laboratory-accelerated ASR studies in a reliable and representative way for investigating ASR damage progression;

d) the analysis of the time series of X-ray tomograms shows that cracks may be first generated inside the aggregates and only afterwards may further propagate into the cement paste. Such further propagation is accompanied by the simultaneous extrusion of ASR products;

The combination of XTM and Cs doping offers an exceptional opportunity to investigate the ASR mechanisms (within the spatial resolution range of XTM).

In this article, only a preliminary and qualitative analysis of the results was presented. Ongoing work focuses on the quantitative analysis of the tomographic time series of segmented cracks and ASR products in order to improve the understanding of ASR and the related cracking in concrete.

6. ACKNOWLEDGMENTS

This work was funded by the Swiss National Science Foundation (SNF), Sinergia project Nr. 171018 (http://p3.snf.ch/project-171018, "Alkali-silica reaction in concrete "). The 3D image analysis was performed by the use of the Empa Platform for Image Analysis, maintained at Empa's Center for X-ray Analytics.

7. REFERENCES

[1] Rajabipour F, Giannini E, Dunant C, et al (2015) Alkali-silica reaction: Current understanding of the reaction mechanisms and the knowledge gaps. Cem Concr Res 76:130–146. https://doi.org/10.1016/j.cemconres.2015.05.024

[2] Chappex T, Scrivener K (2012) Alkali fixation of C-S-H in blended cement pastes and its relation to alkali silica reaction. Cem Concr Res 42:1049–1054. https://doi.org/10.1016/j.cemconres.2012.03.010

[3] Leemann A, Lörtscher L, Bernard L, et al (2014) Mitigation of ASR by the use of LiNO3 - Characterization of the reaction products. Cem Concr Res 59:73–86. https://doi.org/10.1016/j.cemconres.2014.02.003

[4] Chappex T, Scrivener KL (2012) The Effect of Aluminum in Solution on the Dissolution of Amorphous Silica and its Relation to Cementitious Systems. J Am Ceram Soc n/a-n/a. https://doi.org/10.1111/jace.12098

[5] Fernandes I (2009) Composition of alkali-silica reaction products at different locations within concrete structures. Mater Charact 60:655–668. https://doi.org/10.1016/j.matchar.2009.01.011

[6] Thaulow N, Jakobsen UH, Clark B (1996) Composition of alkali silica gel and ettringite in concrete railroad ties: Sem-edx and x-ray diffraction analyses. Cem Concr Res 26:309–318. https://doi.org/10.1016/0008-8846(95)00219-7

[7] Marinoni N, Voltolini M, Mancini L, et al (2009) An investigation of mortars affected by alkali-silica reaction by X-ray synchrotron microtomography: A preliminary study. J Mater Sci 44:5815–5823. https://doi.org/10.1007/s10853-009-3817-9

[8] Guo S, Dai Q, Sun X, Xiao X (2017) X-ray CT characterization and fracture simulation of ASR damage of glass particles in alkaline solution and mortar. Theor Appl Fract Mech 92:76–88. https://doi.org/10.1016/j.tafmec.2017.05.014

[9] Voltolini M, Marinoni N, Mancini L (2011) Synchrotron X-ray computed microtomography investigation of a mortar affected by alkali-silica reaction: A quantitative characterization of its microstructural features. J Mater Sci 46:6633–6641. https://doi.org/10.1007/s10853-011-5614-5

[10] Marinoni N, Voltolini M, Broekmans MATM, et al (2015) A combined synchrotron radiation micro computed tomography and micro X-ray diffraction study on deleterious alkali-silica reaction. J Mater Sci 50:7985–7997. https://doi.org/10.1007/s10853-015-9364-7

[11] Yang S, Cui H, Poon CS (2018) Assessment of in-situ alkali-silica reaction (ASR) development of glass aggregate concrete prepared with dry-mix and conventional wet-mix methods by X-ray computed micro-tomography. Cem Concr Compos 90:266–276. https://doi.org/10.1016/j.cemconcomp.2018.03.027

[12] Lusic H, Grinstaff MW (2013) X-ray-computed tomography contrast agents. Chem. Rev. 113:1641–1666

[13] Chen H, Rogalski MM, Anker JN (2012) Advances in functional X-ray imaging techniques and contrast agents. Phys. Chem. Chem. Phys. 14:13469–13486

[14] Leemann A, Münch B (2019) The addition of caesium to concrete with alkali-silica reaction: Implications on product identification and recognition of the reaction sequence. Cem Concr Res 120:27–35. https://doi.org/10.1016/j.cemconres.2019.03.016

[15] Nightingale ER (1959) Phenomenological theory of ion solvation. Effective radii of hydrated ions. J Phys Chem 63:1381–1387. https://doi.org/10.1021/j150579a011

[16] Feldkamp LA, Davis LC, Kress JW (1984) Practical cone-beam algorithm. J Opt Soc Am A 1:612. https://doi.org/10.1364/josaa.1.000612

[17] Tschumperlé D, Deriche R (2005) Vector-valued image regularization with PDEs: A common framework for different applications. IEEE Trans Pattern Anal Mach Intell 27:506–517. https://doi.org/10.1109/TPAMI.2005.87

[18] Tschumperlé D, Deriche R (2007) Anisotropic Diffusion Partial Differential Equations for Multichannel Image Regularization: Framework and Applications. Adv. Imaging Electron Phys. 145:149–209

[19] Münch B (2019) No Title Xlib (ImageJ / Fiji plugins). In: ImageJ. https://imagej.net

[20] Marstal K, Berendsen F, Staring M, Klein S SimpleElastix: A user-friendly, multi-lingual library for medical image registration

[21] Lowekamp BC, Chen DT, Ibáñez L, Blezek D (2013) The Design of SimpleITK. Front Neuroinform 7:. https://doi.org/10.3389/fninf.2013.00045

[22] Dougherty ER, Lotufo RA (2003) Hands-on Morphological Image Processing. SPIE

[23] Wadell H (1935) Volume, Shape, and Roundness of Quartz Particles. J Geol 43:250–280. https://doi.org/10.1086/624298

[24] Alnaggar M, di Luzio G, Cusatis G (2017) Modeling time-dependent behavior of concrete affected by Alkali Silica Reaction in variable environmental conditions. Materials (Basel) 10:471. https://doi.org/10.3390/ma10050471

[25] Cho HC, Ju H, Oh JY, et al (2016) Estimation of concrete carbonation depth considering multiple influencing factors on the deterioration of durability for reinforced concrete structures. Adv Mater Sci Eng 2016:. https://doi.org/10.1155/2016/4814609